atmosphere

MDPI

Article

Modeling Streamflow Enhanced by Precipitation from Atmospheric River Using the NOAA National Water Model: A Case Study of the Russian River Basin for February 2004

Heechan Han [1], Jungho Kim [2,3,*], V. Chandrasekar [2], Jeongho Choi [4] and Sanghun Lim [5]

1 Department of Civil and Environmental Engineering, Colorado State University, Fort Collins, CO 80523, USA
2 Cooperative Institute for Research in the Atmosphere (CIRA), Colorado State University, Fort Collins, CO 80523, USA
3 NOAA Earth System Research Laboratory, Physical Sciences Division, Boulder, CO 80305, USA
4 Department of Mechatronics Engineering, Chosun College of Science and Technology, Gwangju 61453, Korea
5 Water Resources Research Division, Korea Institute of Construction Technology, Ilsanseo-gu, Goyang-si 10223, Korea
* Correspondence: jungho.kim@colostate.edu; Tel.: +1-970-491-7580

Received: 23 May 2019; Accepted: 12 August 2019; Published: 14 August 2019

Abstract: This study aims to address hydrological processes and impacts of an atmospheric river (AR) event that occurred during 15–18 February 2004 in the Russian River basin in California. The National Water Model (NWM), a fully distributed hydrologic model, was used to evaluate the hydrological processes including soil moisture flux, overland flow, and streamflow. Observed streamflow and volumetric soil water content data were used to evaluate the performance of the NWM using various error metrics. The simulation results showed that this AR event (15–18 February 2004) with a long duration of precipitation could cause not only deep soil saturation, but also high direct runoff depth. Taken together, the analysis revealed the complex interaction between precipitation and land surface response to the AR event. The results emphasize the significance of a change of water contents in various soil layers and suggest that soil water content monitoring could aid in improving flood forecasting accuracy caused by the extreme events such as the AR.

Keywords: atmospheric rivers; flood; hydrological impact; National Water Model

1. Introduction

An atmospheric river (AR), suggested by Reference [1], represents relatively long, narrow flows of precipitable water that move like a river, transporting water vapor from the tropical regions to outside of the mid-latitudes [2–4]. An AR is typically several thousand kilometers long and several hundred kilometers wide and may have a flow of water greater than that of the Amazon River, which is the largest river in the world [2]. ARs were observed in the United States (US) [5–7], Europe [8,9], and Asia [10–12]. In California, along the west coast of the US, AR impacts are a double-edged sword [13]; ARs account for approximately half of the state's annual precipitation and are a vital water supply source for this region where frequent droughts occur, but ARs also cause frequent flood damage by triggering exceptionally heavy rainfall. Along the US west coast, the interaction of AR water vapor transport with steep orographic terrain often leads to complex heavy rainfall events with multiple pulses of intense rain embedded in a background of more uniform stratiform precipitation. The continuous supply of the AR water vapor has considerable hydrologic effects by causing precipitation of a very long duration [14].

The AR event that affected the San Francisco Bay area in 2004 illustrates the possible scale of the impact of a single AR [5]. It brought heavy rains with strong winds, causing damage such as coastal and inland inundations, road closures, air traffic controls, and landslides in several areas. ARs are expected to cause more extreme weather phenomena around the world by the end of the 21st century. According to a recent report by the National Aeronautics and Space Administration (NASA) [15], if greenhouse gases continue to be emitted at the current rate, ARs will become 25% wider and longer than they are now. They also projected that AR phenomena will happen more frequently around the world and, as a result, extreme precipitation and storm events will increase by approximately 50%. This is also a message urging for more research to better understand the hydrologic impacts from extreme weather events enhanced by ARs that are expected to increase in the future.

There was an increase in the number of studies addressing the background, movement, and hydrometeorological characteristics and effects of ARs in the western US [5,7,16–18], central US [19,20], and other countries [4,12,21] where flood damage caused by ARs is becoming more frequent. Some studies examined the hydrological impacts of ARs based on observation data [14,22,23]. These studies investigated the effects of precipitation enhanced by ARs on the near surface moisture flux and runoff flow. In particular, 43% of the annual maximum floods between 1979 and 2009 were caused by ARs, of which 25% had frequencies exceeding 10 years [14].

The National Oceanic and Atmospheric Administration (NOAA) is carrying out the Advanced Quantitative Precipitation Information (AQPI) project to assess potential improvements in precipitation monitoring and short-term forecasts using new high-resolution radar systems to supplement Next-Generation Radar (NEXRAD) coverage over the San Francisco (SF) Bay urban region. The AQPI information is expected to aid water agencies in the nine counties in the SF Bay area to mitigate flood damage by extreme heavy rain events including ARs [24,25]. The AQPI system will also assess the impact of high-resolution precipitation on hydrologic forecasts from the NOAA National Water Model (hereinafter referred to as NWM) which is in operation throughout the US since 2016. The NWM has a high resolution (1 km) and is expected to be especially useful to water agencies for small watersheds that currently have no hydrologic information. Because the NWM is physically based, the model can be used to better understand the linkage between land surface and surface flow processes. The NWM is expected to overcome the physical limitations (e.g., deep soil flux analysis and hyper-resolution-based surface flow tracking) of observation-based analysis in terms of understanding the hydrological processes.

The high-resolution hydrological products generated by a hydrological model provide a basis for the spatiotemporal analysis of the hydrological impacts. For the AR events, it is critical to examine the effects on various hydrological processes due to the AR heavy rainfall occurrence characteristics that are different from general heavy rainfall events. This study aims to introduce the NWM in the NOAA hydrological prediction system, which is to mitigate flood damage by extreme heavy rain events enhanced by the ARs as part of the AQPI project. For this purpose and as a case study, hydrological products simulated by the NWM are introduced and validated using an AR event which caused considerable damage to California state in the United States. The case study is to present a brief overview of the NWM performance to streamflow and soil moisture simulations. In the performance review, the suitability of the NWM for AR analysis is examined by comparing the simulated soil water contents and streamflows produced by the NWM with the observed data. The impacts of the AR on hydrological processes that occurred on 15–18 February 2004 are examined using various hydrological outputs from the NWM including volumetric soil water content, direct runoff, and streamflow. The target area of this study is the Russian River basin in north San Francisco, California.

This paper is composed of four sections including the Introduction and Conclusions. Section 1 describes the background and purpose of this study. Section 2 explains the background knowledge of AR and the methodology of the NWM. Section 3 outlines the verification results for the model and the analysis results of the hydrological impacts of AR events. Finally, Section 4 summarizes the conclusions derived from this study.

2. Materials and Methods

2.1. Atmospheric River

ARs represent narrow atmospheric bands of water vapor transports that mainly occur in the air of the midlatitudes [1]. According to Reference [4], ARs not only contain a large amount of water vapor and feature strong low-level winds, but they also form part of the warm conveyor belt of an extratropical cyclone (Figure 1). ARs are known as a cause of fatal floods and landslides due to the continuous inflow of vapor leading to large amounts of precipitation for a long duration.

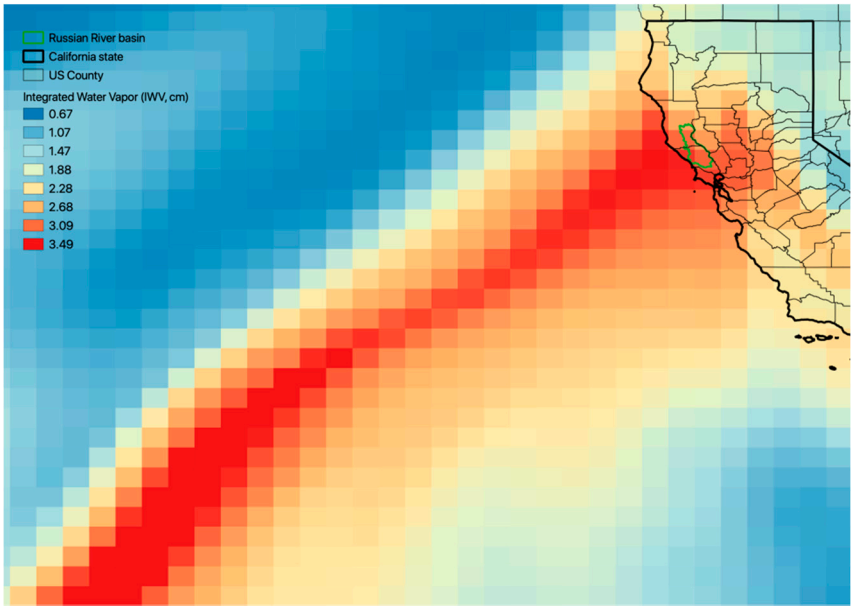

Figure 1. Integrated water vapor (cm) carried by the atmospheric river of 15 February 2004 on the west coast of the United States (US).

There are two typical methods of detecting ARs. The first method is based on the detection of the integrated water vapor (IWV). An AR is defined as a water vapor transport where the cross-section of a 2-cm or larger IWV plume is narrower than 1000 km and longer than 2000 km [3]. The second method is based on the detection of the vertically integrated water-vapor transport (IVT). An AR is defined as having an IVT $\geq$250 kg·m^{-1}·s^{-1} that occurs in an area where the atmospheric pressure is between 300 and 1000 hPa [2]. The thresholds required for the AR detection can be determined using remote sensing data acquired from satellites, zonal and meridional vapor flux reanalysis data, and AR models.

2.2. National Water Model

The NWM is a high-resolution hydrological model run over the conterminous US (CONUS) to enhance hydrologic forecasting capabilities at different lead times. The core of the NWM system is the National Center for Atmospheric Research (NCAR)-supported community Weather Research and Forecasting Hydrologic model (WRF-Hydro). The NWM delivers streamflow forecasts on the 2.7 million river reaches of the United States Geological Survey (USGS) NHDPlus v2 hydrography dataset, as well as gridded analyses of a host of other hydrologic variables (e.g., soil water contents at various depths). The NWM simulates the water cycle with mathematical representations of the different hydrologic and land surface processes and how they fit together to distribute water at the surface and subsurface [26]. Figure 2 shows the hydrological architecture and hydrologic processes included in the NWM. The model includes a forcing engine for handling various data (e.g., precipitation rate, surface pressure, short and long-wave radiations, vertical and horizontal winds, temperature, and specific humidity), land surface model for soil flux, terrain routing for hillslope surface flows, channel routing

based on the National Hydrography Dataset (NHD) plus a channel network, and a reservoir inflow and outflow simulation process. This complex representation of physical processes such as snowmelt and the infiltration and movement of water through the soil layers varies significantly with changes in various factors such as the elevation, soil, and vegetation. Additionally, extreme variability in the amount of precipitation over short distances and times can cause the responses of rivers and streams to change very quickly. For the detailed methodology background, readers can refer to the WRF-hydro technical description and user's guide [27].

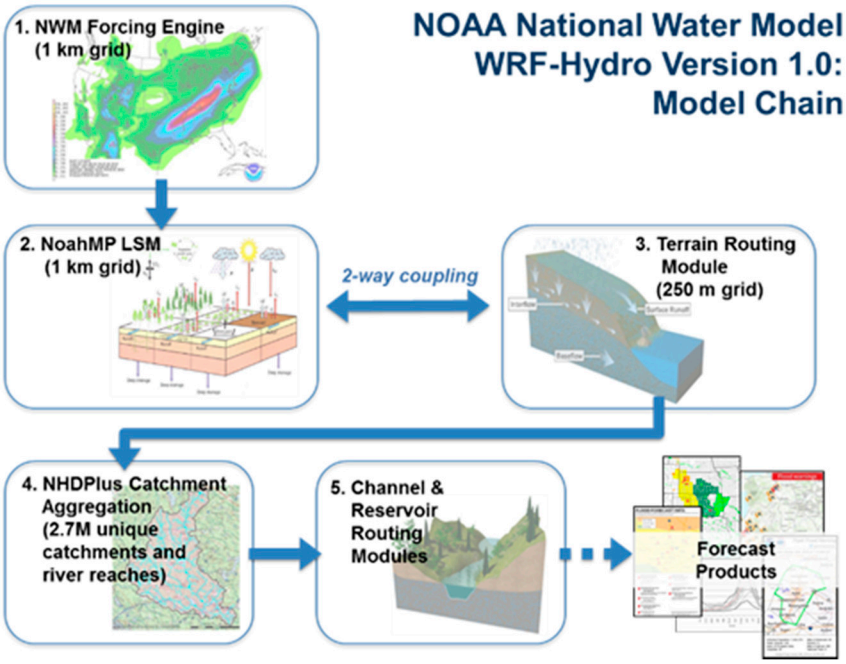

Figure 2. Diagram of complex hydrological processes of the National Water Model (NWM) [28].

The forcing engine ingests the requisite hydrologic forcing from a variety of sources including multi-radar/multi-sensor system (MRMS) radar-gauge observed precipitation data, high-resolution rapid refresh (HRRR), rapid refresh (RAP), global forecasting system (GFS), and climate forecast system (CFS) numerical weather prediction (NWP) forecast data. WRF-Hydro is configured to use the Noah-MP Land Surface Model (LSM) to simulate land surface processes. Separate water routing modules perform diffusive wave surface routing and saturated subsurface flow routing on a 250-m grid, and Muskingum–Cunge channel routing down National Hydrography Dataset (NHDPlusV2) stream reaches. River analyses and forecasts are provided across a domain encompassing the CONUS and hydrologically contributing areas, while the land surface output is available for a larger domain extending beyond the CONUS into Canada and Mexico (roughly from latitude 19° north (N) to 58° N). The system includes analysis and assimilation configuration along with three forecast configurations. The USGS streamflow observations are assimilated into the analysis and assimilation configuration, and all four configurations benefit from the inclusion of 1260 reservoirs.

2.3. Hydrological Products Provided by NWM

Various hydrological products (e.g., soil water content, direct runoff, and streamflow) of the NWM provided by the NOAA National Water Center are used. The NWM hydrologic products used in this study were from a standalone simulation which was not coupled to an atmospheric model as it was a retrospective analysis simulation based on observed meteorological forcings. The land data assimilation system's meteorological forcings are used as inputs and 1992 is used as the spin-up period. The hydrological products are public to all users and are available at Environmental

Data Commons (http://edc.occ-data.org/nwm/getdata/#archive-data-access). It provides streamflow (an hourly time step for each channel segment), lake and reservoir-related products (an hourly time step for each waterbody), land surface model outputs (three-hourly time step and 1-km resolution), and ponded water depth and soil saturation outputs (three-hourly time step and 0.25-km resolution). These products are available for 25 years (1 January 1993–31 December 2017).

Hydrological products (HP) are required to represent complex hydrological processes. Table 1 lists the features of the HPs generated by the NWM. The LSM uses 1.0-km grids and generates the simulation results for the HPs. HPs corresponding to grid data include volumetric soil water content, evapotranspiration, and snow-related variables. The soil water content is provided for a total of four soil layers (layer-1: 0–100 mm; layer-2: 100–400 mm; layer-3: 400–1000 mm; layer-4: 1000–2000 mm), making it possible to examine the flux between the top soil layer and the deep soil layer. HPs based on 250-m grids include ponded water depth, which represents the direct runoff, and depth to soil saturation, which represents the saturation state of the soil.

Table 1. Features of hydrological products produced by the National Water Model (NWM).

Type	Size	Variable	Unit	Others
Grid	1 km	Soil moisture saturation for four layers	fraction	Volumetric soil water content (m^3/m^3)
		Accumulated evapotranspiration	mm	-
		Snow temperature	K	-
		Column-averaged snow cover fraction	fraction	-
		Snow water equivalent	km/m^2	-
		Snow depth	m	-
	250 m	Ponded water depth	mm	Direct runoff depth
		Depth to soil saturation	m	-
Point	-	Streamflow	m^3/s	Discharge
		Velocity	m/s	-
		Channel inflow	m^3/s	Discharge
		Reservoir elevation/inflow/outflow	m and m^3/s	Water level and discharge

The HPs corresponding to point data include the discharge, velocity, and channel inflow stream of each channel segment. Reservoir HPs include the water level, which is a state variable, inflow discharge to the reservoir, and outflow, which is the released water.

In this study, the simulated streamflow data (hourly) during 15–18 February 2004 and simulated soil water content data (three-hourly) from the NWM for 2017 were used for NWM verification. Also, hydrological outputs (soil moisture saturation, ponded water depth, and streamflow) provided by NWM were used to analyze the hydrological impact of the AR (15–18 February 2004).

2.4. Data

2.4.1. Study Area

The Russian River basin straddles Sonoma and Mendocino Counties in California (Figure 3). The basin has a drainage area of approximately 3,465 km^2 above USGS gauge 11467000. Figure 3a shows the accumulated precipitation map of the target AR event resulted from the tropical rainfall measuring mission (TRMM). The event primarily impacted northern California and generated a total precipitation of 146 mm in the Russian River basin. Note that the 146-mm total represents an average across the watershed. The amounts of total rainfall vary considerably across the basin due to orographic enhancement of precipitation in the higher-terrain regions compared to the low-lying areas, consistent with previous studies of precipitation in this area [24,29–31]. This precipitation event caused

heavy runoffs on the Russian River, which exceeded flood level at Guerneville on 18–19 February 2004 [5]. Also, the occurrence of AR events leading to extreme precipitation is not a one-time event but a phenomenon observed several times each year. According to Reference [32], 65 AR events were observed in the California coast area between 2005 and 2008.

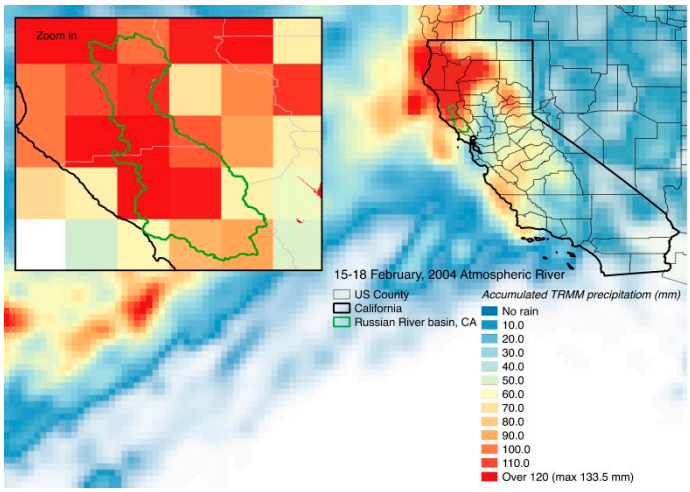

(**a**) Accumulated precipitation (mm) for 15–18 February 2004 in the Russian River basin and California.

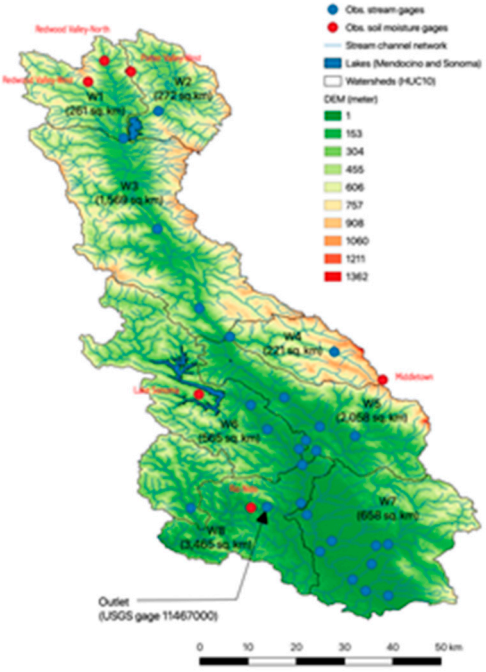

(**b**) Observation gauge (streamflow and soil moisture) locations and watersheds on digital elevation model (DEM).

Figure 3. Total precipitation and characteristics of the Russian River basin. Watersheds (referred to as "W") indicate the hydrologic unit code 10 determined by the United States Geological Survey (USGS).

Figure 3b shows the USGS gauge locations and stream channel network on a digital elevation model (DEM). The elevations within the drainage area range from 24 m at the gauge outlet near the Pacific Ocean to 880 m at the headwaters along the eastern edge of the basin. Higher elevations within the basin are characterized by forested areas with some concentrated areas of rangeland. Major cities along the Russian River include Ukiah (population 16,075) and Healdsburg (population 11,254). In the

Russian River basin, there are two lakes, Mendocino and Sonoma, which are critical to providing flood control and supplying water to meet water usage requirements and minimum stream flows. The lakes are regulated by the Coyote Valley Dam and Warm Springs Dam, respectively.

In addition, the NWM was updated as several versions such as 1.1 and 1.2 (for this study), and the updates include new watersheds calibrated. However, the calibration process for the Russian River basin is underway. Kim et al. [33] evaluated the NWM retrospective performance in the San Francisco Bay area for five years (2013–2017 year). Although the study was not able to address the NWM performance depending on the watersheds calibrated, it confirmed that the NWM performance in the Russian River basin varies with watershed sizes, regulations by hydrologic facilities, and storm features.

2.4.2. Observation Data

Table 2 lists the USGS stream gauges and soil water content observatories in the Russian River basin used to verify the performance of the model. The gauges represent sub-basin areas ranging from a few tens of kilometers to several thousand kilometers. Of the ten gauge sites in Table 2, six are located in relatively natural regions, which are not regulated by hydrologic structures, with sub-basin size ranging up to a few hundred square kilometers. The remaining four sites are larger and are located in sub-basins regulated by upstream reservoirs. In the case of the soil water content, six observation points were used to evaluate the model performance. The points represent elevation ranging 39–972 m and provide the observed soil water content data for a soil depth of 10 cm. The Russian River basin is subject to periodic flooding by ARs due to a combination of its geographical location along the US west coast and the result of steep terrain in the watershed. Parameter-Elevation Regressions on Independent Slopes Model (PRISM) data [34] state that the average annual precipitation in the basin ranges from about 938 to 1635 mm, and 83% of the annual average precipitation occurs during the wet season (generally, November–March).

Table 2. United States Geological Survey (USGS) stream gauges and soil water content observation sensors used in this study. ID—identifier; N/A—not applicable.

Station ID (USGS)	Drainage Size (km^2)	Elevation (m)	Location		Flow Type	Lake	Available Period
			Latitude (°)	Longitude (°)			
11467000	3465.4	6.2	38.5086	−122.9266	Regulated	Mendocino/ Sonoma	October 1987
11464000	2053.9	23.9	38.6133	−122.8352	Regulated	Mendocino	October 1987
11463000	1302.8	N/A	38.8790	−123.0530	Regulated	Mendocino	October 1989
11462500	937.6	154.3	39.0270	−123.1310	Regulated	Mendocino	October 1987
11461000	259.0	185.8	39.1960	−123.1940	Natural	N/A	November 1987
11461500	238.8	244.2	39.2466	−123.1291	Natural	N/A	October 1987
11466320	201.0	N/A	38.4452	−122.8061	Natural	N/A	December 1998
11467200	162.7	12.4	38.5066	−123.0686	Natural	N/A	October 2003
11466200	147.6	31.0	38.4366	−122.7236	Natural	N/A	December 2001
11463170	33.9	4.1	38.7977	−122.8013	Natural	N/A	October 1987
Site Name (Soil Water Content Observation)			**Latitude (°)**	**Longitude (°)**	**Elevation (m)**	**Observation Start Date**	
Lake Sonoma			38.7187	−123.0537	396	17 December 2010	
Middletown			38.7456	−122.7112	972	10 December 2014	
Potter Valley—West			39.3204	−123.1801	518	26 May 2016	
Rio Nido			38.5073	−122.9565	39	2 December 2006	
Redwood Valley—North			39.3406	−123.2297	294	25 May2016	
Redwood Valley—West			39.3014	−123.2601	631	26 May 2016	

3. Results

3.1. Model Verification

The streamflow simulation results were evaluated using the hourly observed streamflow data for the ten USGS stations. The period of the verification date was from 15 to 18 February 2004. Figure 4

shows the box–whisker plots for the simulation results of five error indices, namely, the correlation coefficient (CC), Nash–Sutcliffe efficiency (NSE), percent bias (PBIAS), peak flow (PF), and time to peak (TP) errors. The equations of the error indices are as shown below (Table 3).

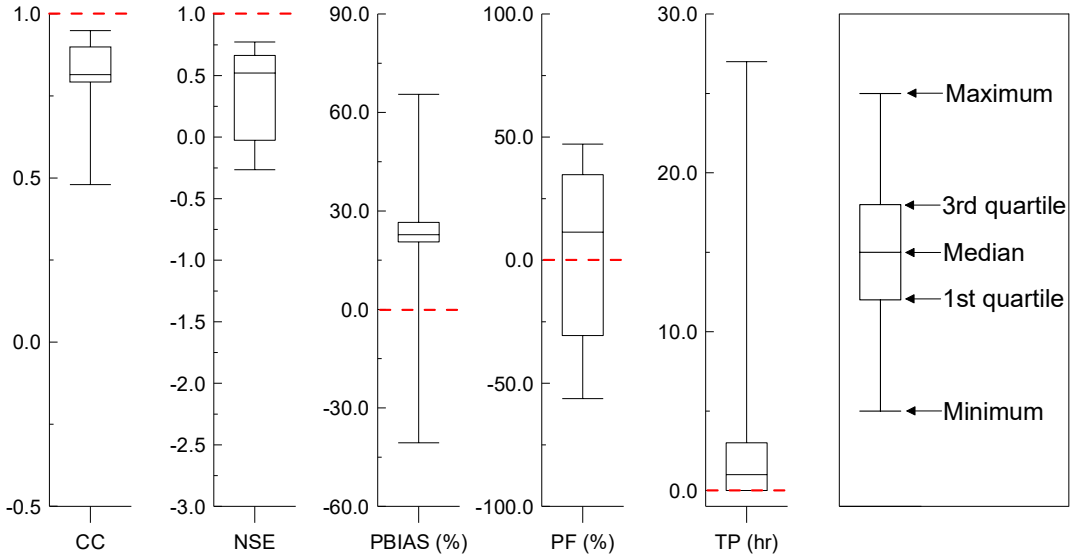

Figure 4. Box–whisker plots of error indices for evaluation of the NWM performance. The hourly streamflow data (15–18 February 2004) and five indices (correlation coefficient (CC), Nash–Sutcliffe efficiency (NSE), percent bias (PBIAS), peak flow (PF) (%), and time to peak (TP) (h)) were used for evaluation. These plots show the distribution of the values of error of simulated streamflow data. The red spotted line means the ideal value of each index (e.g., simulated value is perfectly fit to the observation).

Table 3. Statistics for evaluation of NWM simulation results.

Error Indices	Acronym	Equation
Correlation coefficient	CC	$\frac{\sum (Q_{sim}-\overline{Q_{sim}})(Q_{obs}-\overline{Q_{obs}})}{\sqrt{\sum (Q_{sim}-\overline{Q_{sim}})^2}\sqrt{\sum (Q_{obs}-\overline{Q_{obs}})^2}}$
Nash–Sutcliffe efficiency	NSE	$1-\frac{\sum (Q_{sim}-Q_{obs})^2}{\sum (Q_{obs}-\overline{Q_{obs}})^2}$
Percent bias	PBIAS	$(\sum (Q_{obs}-Q_{sim})) \div \sum Q_{obs} \times 100\ (\%)$
Bias	BS	$(\sum Q_{sim} \div \sum Q_{obs}) \times 100\ (\%)$
Time to peak error	TP	$T_{obs} - T_{sim}$
Peak flow error	PF	$((Max(Q_{obs}) - Max(Q_{sim})) \div Max(Q_{obs})) \times 100\ (\%)$

The accuracy of the simulation results was generally high. Most CCs were higher than 0.8, and the NSE ranged from −0.25 to 0.75. In particular, most NSE results were higher than 0.0, indicating that the simulated streamflow exhibited an acceptable level of performance compared to the average of the observed streamflow. For PBIAS, the first to third quantiles belonged to the 15–30% range, indicating a low runoff volume error. The range of error in peak flow was from −50% to 50%, indicating that the model does not simulate the peak flow rate well compared to the observed discharge. The peak time error was also less than 3.5 h in most locations, and the largest error in peak time was about 27 h at one station (e.g., USGS gauge 11463170).

Figure 5 shows the hydrograph of the hourly simulated and observed streamflow data for the ten stations. Most hydrographs show that NWM simulated the tendency properly but there were

differences between peak flows. The overall coefficient of determination (R-squared, R^2) was found to be 0.65 and the range of R^2 was 0.23–0.91 for the 10 stations.

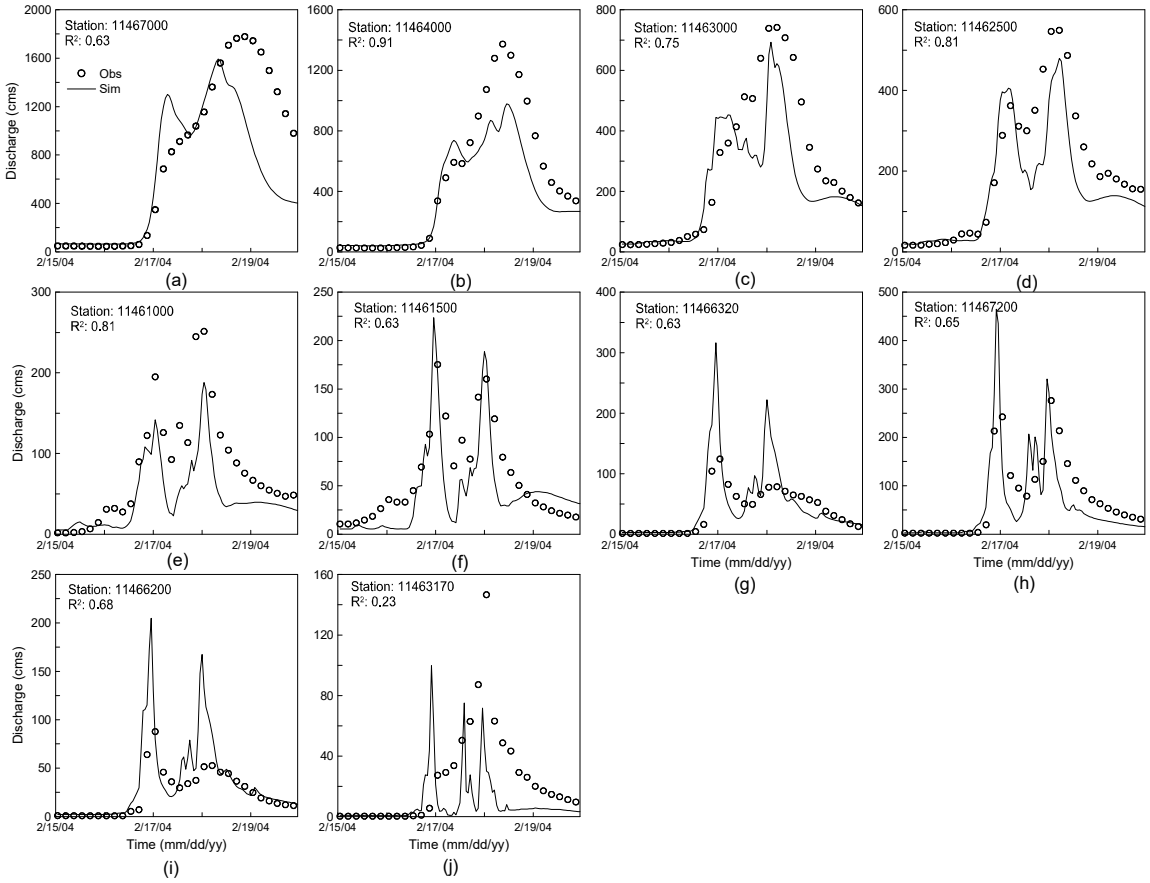

Figure 5. Comparison of hourly observed (USGS) and simulated (NWM) streamflow data at the ten stations (15–18 February 2004). The line means the simulated streamflow by the NWM, and the dot means the observed streamflow at each station. (**a**–**j**) are ten stations in the Russian River basin listed in Table 2.

The difference in the results was found according to the reservoir operation effect and drainage area. In the stations affected by reservoirs and dams (Figure 5a–c), the observed hydrograph was a single peak, whereas two or more peak flows were simulated from the NWM. Reservoirs and dams reduce the peak flow in the downstream area by storing the runoff from the upstream area for flood control during the storm period. On the other hand, since the reservoir representation scheme of the present NWM does not reflect the actual reservoir operation, it discharges the reservoir inflow to the downstream. As a result, the simulated discharge was overestimated when the water was not actually discharged from the dam. However, the difference between two flows was not relatively large, and trends in flow and peak time were properly simulated. The average CC for these points was 0.88, R^2 was 0.78, and TP was less than 2 h.

In the case of watersheds with an area less than 1000 km^2 (Figure 5d–j), the NWM simulated the trends well even though the observed hydrographs were complex, consisting of two or more peak flows. The average CC for these points was 0.77, R^2 was 0.61, and TP was less than 5 h. Since calibration for the Russian River basin of the NWM is underway, calibration of parameters related to the antecedent soil moisture and direct runoff needs to be performed. In particular, the error indices at station 11463170 were 0.48 for CC, 0.23 for R^2, and 27 h for TP, showing the poorest simulation results among the target stations. In addition, this station has the smallest drainage area and the steepest slope.

In this study, six situ soil water content data in the Russian River basin were manipulated to evaluate the soil flux estimation performance of the NWM. Since all of the soil water content sensor data in the Russian River basin were not available for the AR event in 2004 but available from 2016 onward, the data observed from 1 January–31 December 2017 were used to compare with the NWM results. CC, NSE, and bias (BS) were used as the three error indices for evaluation. Figure 6 shows the time series and error indices (CC, NSE, and BS) for three-hourly soil water content. All error indices were found to vary with season, and the difference in soil water content modeling performance between the wet season (January–March and November–December) and dry season (April–October) was evident. Also, the results of BS show that simulation performance was better in the wet season than dry season when AR was frequently generated. In the wet season, the bias caused by the dramatic changes in the soil water content were observed at Potter Valley—West, Rio Nido, and Redwood Valley—North points, and the differences between the peak flow were also evident. In the case of Lake Sonoma, BS showed 159.3%, indicating that the difference between observation and simulated results was significant compared to other sites. In the dry season, soil water content was predominantly attenuated, and the error between observation and simulated results was mostly due to bias. In particular, errors were apparent in Lake Sonoma (BS 314.8%) and Rio Nido (BS 207.6%).

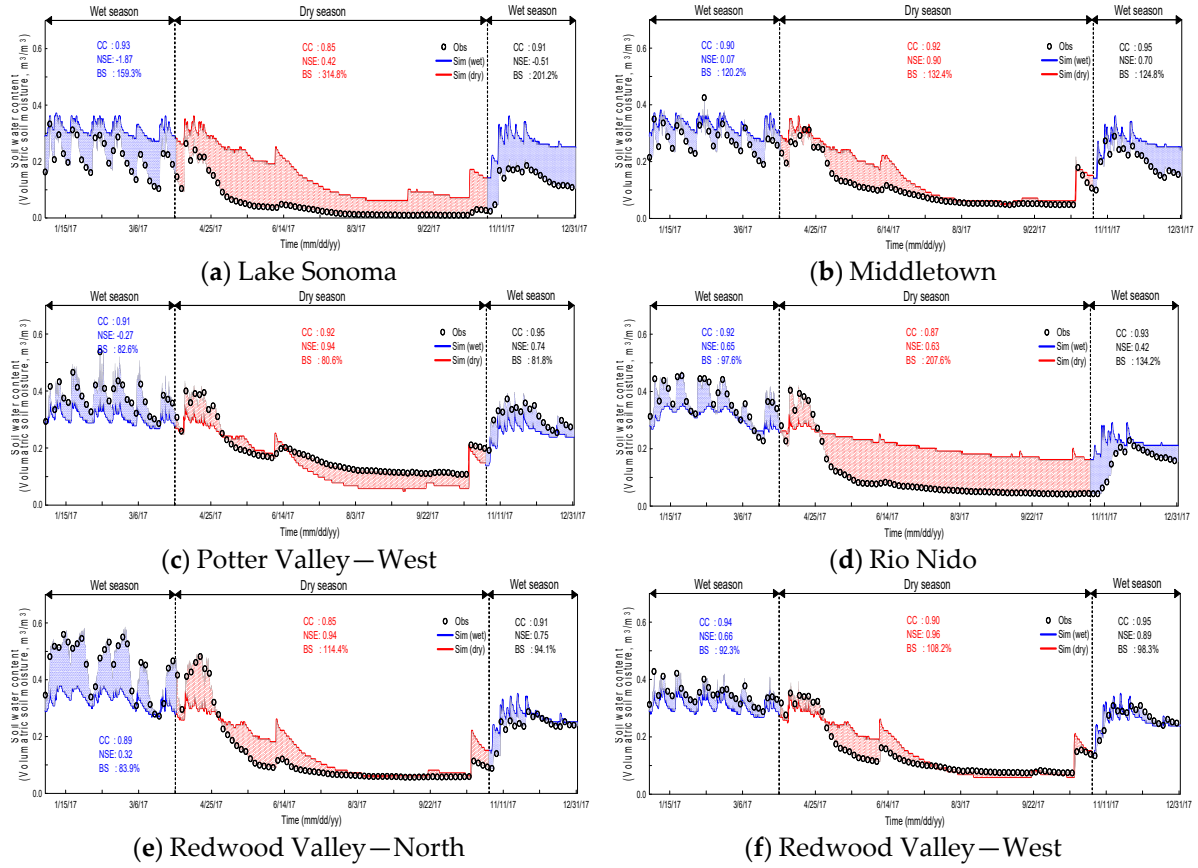

Figure 6. Comparison of three-hourly observed and simulated soil water content data at the six stations for 2017. Blue and red lines mean simulated soil water content during wet and dry seasons, respectively, and dots indicate the observed soil water content data. (**a**–**f**) are six stations in the Russian River basin listed in Table 2.

3.2. Hydrological Impacts of the Atmospheric River

3.2.1. Overview

Figure 7 shows the observed IWV which was obtained from the NASA Modern-Era Retrospective Analysis for Research and Application (MERRA) reanalysis, as well as precipitation and time-series results for the soil water content, direct runoff depth (e.g., overland flow), and streamflow as simulated using the NWM for the AR event (15–18 February 2004). The soil water content and direct runoff depth were the area average values across the Russian River basin. The streamflow represents the hourly discharge simulated for every stream channel segment in the basin. For the simulated streamflow, time-series data scaled to the peak flow and non-scaled time-series data for 11467000 (outlet of the Russian River basin) are both shown.

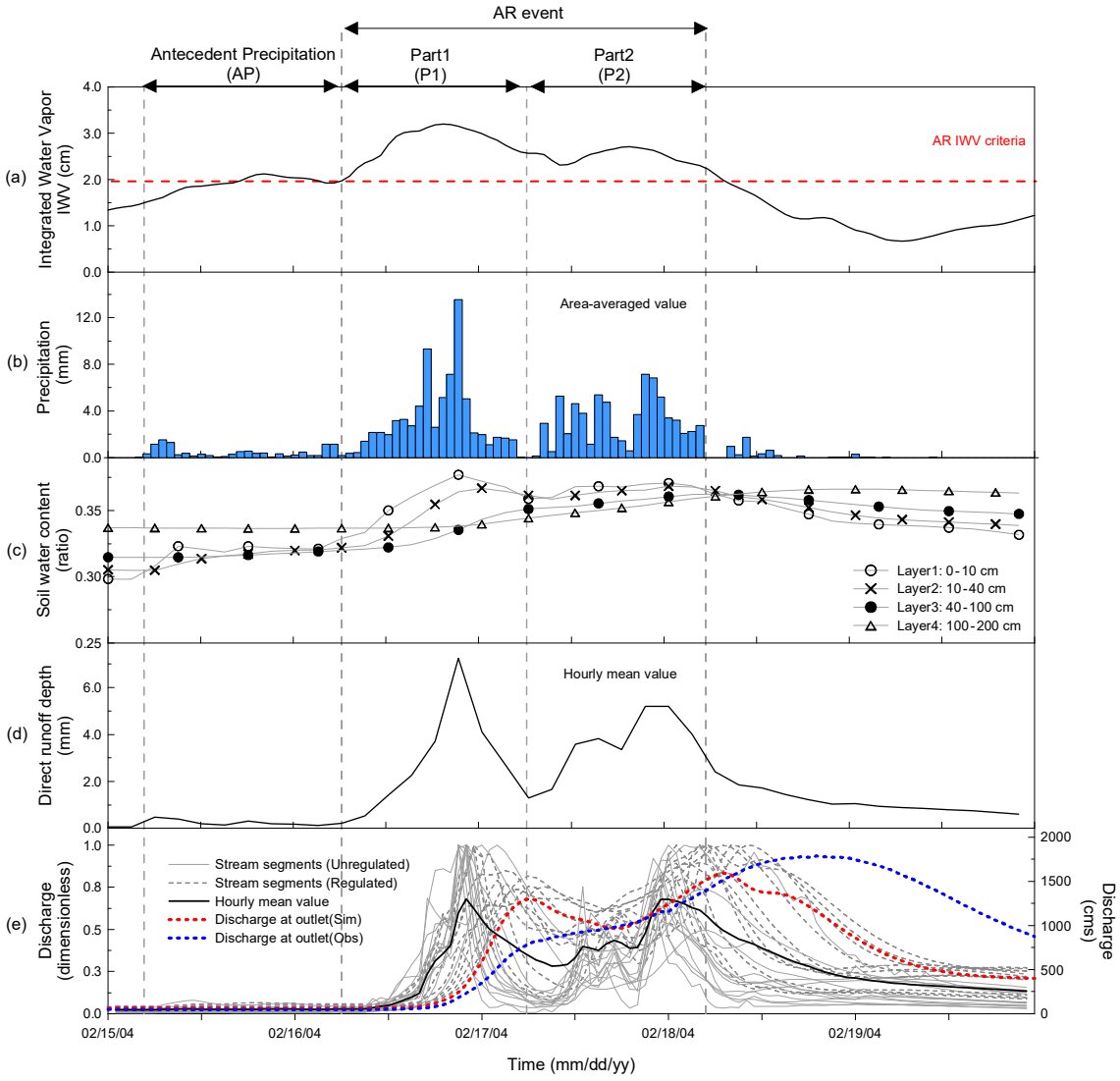

Figure 7. Time-series results obtained with the NWM (15–19 February 2004). The results shown in the figure include the integrated water vapor (cm) (**a**), precipitation (mm) (**b**), soil water content for four layers (**c**), direct runoff depth (mm) (**d**), and streamflow discharge (**e**). The three periods, AP, P1, and P2, indicate the antecedent precipitation time just before the AR event and two parts of the AR event. Simulated results for (**a**–**d**) are area-averaged values over the entire domain, and (**e**) shows the simulated discharge for USGS gauges in each stream.

The four-day event with precipitation occurring everyday encompassed 15–18 February, and AR began its impact on 16 February (IWV slightly above AR criterion of 2 cm—Figure 7a) with some precipitation, but the main story was the two pronounced periods of enhanced precipitation on 16 and 18 February (Figure 7b) corresponding to larger pulses of the IWV above the AR threshold. The precipitation peaks and trend were associated with trends of soil water content of topsoil layers (Figure 7c), direct runoff depth (Figure 7d), and streamflow (Figure 7e). To highlight the hydrological effects associated with different phases of the AR, the four-day time series in Figure 7 (97 h) was divided into three periods (antecedent precipitation (AP), and two time points P1 and P2). The AR precipitation where the IWV exceeded the AR criterion (IWV > 2 cm) occurred for a total of 47 h (8:00 a.m. 16 February–6:00 p.m. 18 February). The AP had a duration of 24 h and 11.4 mm of total precipitation. P1 continued for approximately 24 h, and the maximum hourly precipitation was 13.5 mm/h. P2 continued for approximately 23 h, and the maximum hourly precipitation was 7.13 mm/h. As shown in the figure, the IWV and the precipitation trends were very similar. Furthermore, P1 dominated over P2 in terms of precipitation.

The NWM simulation of soil water content in the four soil layers is shown in Figure 7c. The soil water content simulated from infiltrated precipitation during the AP period affected the soil water content change of soil layers during the P1 period. Soil water content of topsoil layers (layers 1 and 2), which are drier than deep soil layer (layers 3 and 4), gradually increased due to the infiltrated precipitation during the AP period. During the P1 period, precipitation had a major effect on the change in the soil water content in layers 1 and 2 (the top soil layers), but the changes in the soil water content level of layers 3 and 4 (the deep soil layers) were not significant (Figure 7c). The precipitation that infiltrated during the P1 period played the role of increasing the soil water content of the deep soil layer during the P2 period. Unlike during the P1 period, during the P2 period, the soil water content level in layer 4 exhibited an increasing trend, and this led the changes in the upper layers. In particular, the increasing trend in the soil water content of layers 1 and 2 became identical to that of layer 4. This corresponds to the physical phenomenon whereby the percolation rate in the deep soil layers increases as a result of continuous water infiltration, while the infiltration rate of the topsoil layer decreases. The phenomenon is very normal when considering infiltration and percolation rates by time [35]. P1 and P2 showed clear differences in the saturation rate by the soil layer. Table 4 lists the saturation rates (a change in saturation/hour) of the four soil layers by the AR period. In P1, the saturation rates of layers 1 and 2 were higher than 0.05, indicating rapid changes, but the saturation rate of layer 4 was 0.005, indicating almost no change. In P2, the saturation rates of the four soil layers ranged from 0.0103 to 0.0164, indicating a very low variability and generally similar saturation rates. Based on the above results, it was demonstrated that a complex heavy rainfall enhanced by the AR is the most significant threat to floods as it has not only a long duration, but also enough water to saturate soil layers. This feature of AR rainfall events causes changes in the soil water content of the deep soil layer, which plays a role in determining percolation rate, and this decreases the infiltration rate of the topsoil layer due to the interaction with percolation process. Consequently, this process leads rainfall to higher direct runoffs as time progresses.

Table 4. Saturation rates depending on soil layers and atmospheric river (AR) periods. The values are areal averages over the Russian river basin.

Layer	Saturation Rate (Change in Soil Water Content in an Hour)	
	P1	P2
1	0.0527	0.0125
2	0.0597	0.0103
3	0.0340	0.0129
4	0.0052	0.0164

The direct runoff depth (DRD) showed the same increasing and decreasing trends as the hyetograph, and peak values in P1 and P2 (Figure 7d). Table 5 lists the total precipitation, accumulated DRD, and the ratio of DRD to precipitation for the P1 and P2 periods. The mean and maximum precipitation during P1 were 3.1 and 13.5 mm/h, respectively, which were higher than those of P2. However, the accumulated DRD of P2 was 28.1 mm, which was approximately 12% higher than that of P1. Furthermore, the ratio of the accumulated DRD to the total precipitation confirms that the outflow rate in P2 was higher than that in P1 because of the preconditioning of P1. During the P2 period, increased soil water content of the topsoil layers caused high DRD.

Table 5. Features of precipitation and direct runoff depth for P1 and P2. The values are areal averages over the Russian river basin.

Contents	P1 (6:00 a.m. 16 February–5:00 a.m. 17 February)	P2 (6:00 a.m. 17 February–4:00 a.m. 18 February)	Total (6:00 a.m. 16 February–4:00 a.m. 18 February)
Total precipitation (mm) (%)	75.17 (51.45%)	70.93 (48.55%)	146.09 (100%)
Duration (h)	24	23	47
Mean precipitation (mm/h)	3.13	3.08	3.11
Max precipitation (mm/h)	13.54	7.14	13.54
Accumulated direct runoff depth (mm) (%)	22.22 (44.14%)	28.12 (55.86%)	50.34 (100%)
Ratio of direct runoff depth to precipitation	0.296	0.396	0.345

The trend exhibited by the streamflow was very similar to that of the DRD, with peak flows appearing in P1 and P2. The streamflows in each channel segment showed various shapes of hydrographs due to several factors such as flow type, as well as topographic and stream characteristics, and the overall trend was very similar to the ponded water depth. The hydrograph at the basin outlet also exhibited a complex shape with two peak flows. The maximum peak flow occurred during P2, which was the result of the change in the soil water content caused by P1 and a relatively high outflow rate as described above. The additional hydrological impacts of the AR on the soil flux, direct runoff, and streamflow are explained in the following section.

3.2.2. Soil Flux

Figure 8 shows the changes in soil water content level between the initial and peak times during P1 and P2 periods for the four soil layers. The results for the P1 period reveal several important features. Firstly, the change in soil water content level during the P1 period was relatively large in layers 1 and 2, but small in layers 3 and 4. This is because, in layers 1 and 2, which correspond to the topsoil layer (or near-surface soil layers), the change in soil water content level is dominated by the infiltrated precipitation, whereas, in layers 3 and 4, which correspond to the deep soil layers, the change in soil water content level is dominated by percolation. Furthermore, it can be inferred from the large change in the soil water content levels in layers 1 and 2 during the P1 period that the precipitation during the AP was insufficient to saturate the soil.

The change pattern of the soil water content level in the P2 period was different from that in the P1 period. The most notable characteristic was that there were no significant variations in the change in soil water content levels in the four soil layers. This result indicates that the precipitation that infiltrated during the P1 period saturated the topsoil layer. In the deep soil layers, layer 4 was noteworthy. The change in soil water content in layer 4 was greater in P2 than in P1, which means that more soil water content moved to the deeper layer during the P2 period. In other words, in P1, the infiltrated precipitation played the greatest role in changing the soil water content level in the top layers, whereas, in P2, percolation had the greatest effect in the deep layers. In terms of flood analysis, the change in soil water content level during P2 was more significant than that during P1. It is thought

that the precipitation that infiltrated during P1 gave rise to a base flow during P2, thus contributing greatly to the total runoff volume.

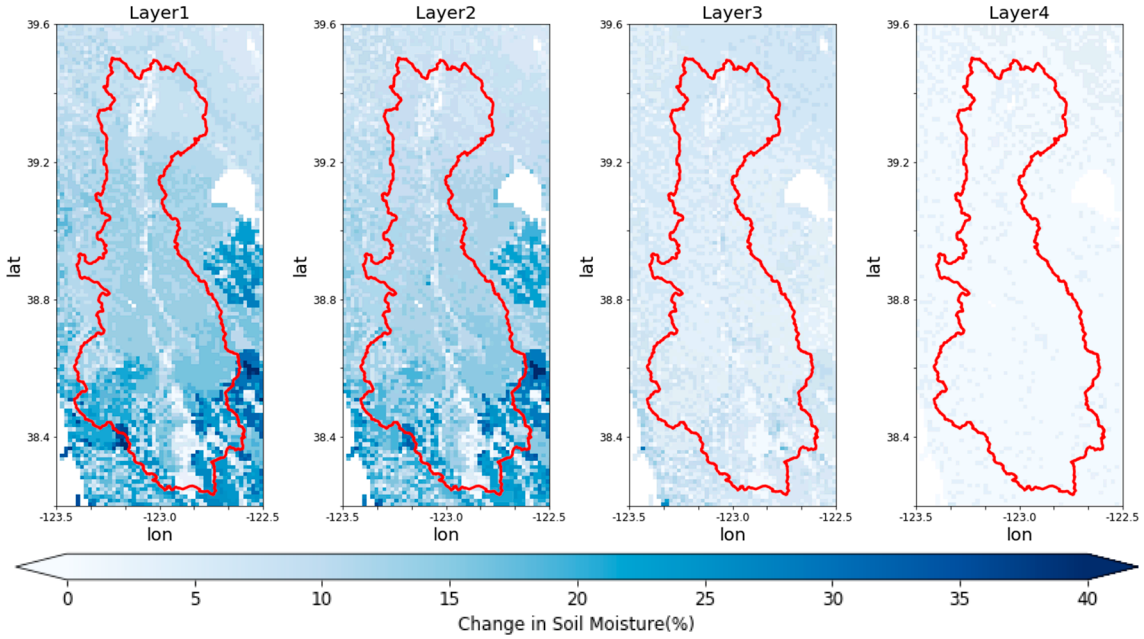

(**a**) Change in soil water content during the P1 period.

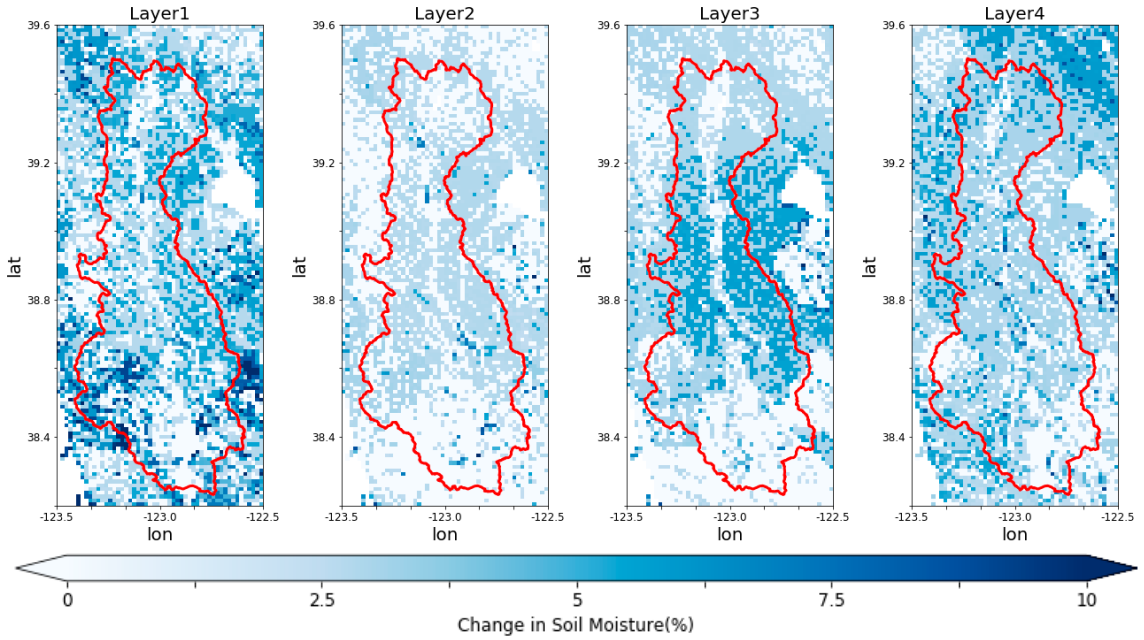

(**b**) Change in soil water content during the P2 period.

Figure 8. Changes in soil water content for each grid cell as the difference between the initial and peak time of the streamflow during (**a**) P1 and (**b**) P2. The ranges of change in soil moisture were 0–40% for P1 and 0–10% for P2.

3.2.3. Surface Flow

Figure 9 shows the DRD at the initial and peak times during P1 and P2. In both P1 and P2, the distribution and size of the DRD did not change much at the peak time, but the depth of the DRD at the initial time in P2 was greater than that in P1 because of the preconditioned soil water content during P1. As indicated by the soil water content results, the precipitation that infiltrated during P1

caused a high direct runoff at the initial time during P2. This result demonstrates that not only the precipitation in P2, but also the precipitation in P1 had direct and indirect effects on the DRD in P2.

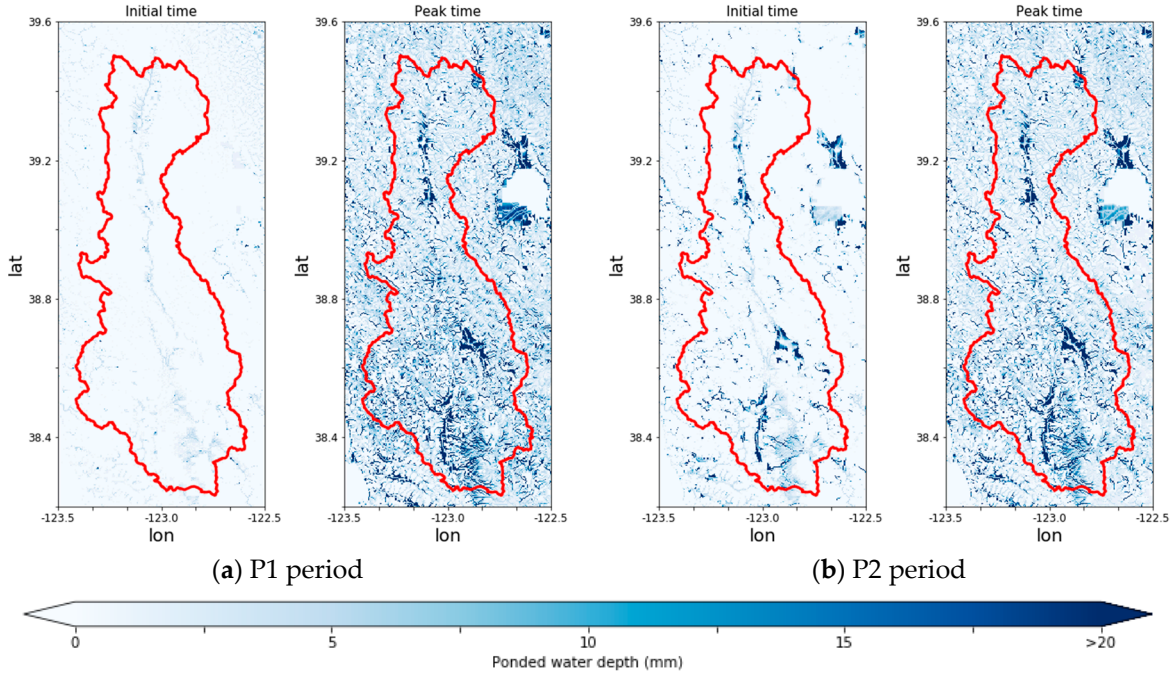

Figure 9. Distribution of direct runoff depths at initial and peak times for (**a**) P1 and (**b**) P2 periods.

The flood frequency of the simulated streamflow was analyzed for eight sub-watersheds in the Russian River basin. For these sub-watersheds, the drainage areas were distinguished based on the hydrologic unit code (HUC) 10, whose average size is 587.9 km^2. Figure 10 shows the peak flows of the eight watersheds and the corresponding T-year recurrence intervals. The flood frequency was estimated using regional regression equations which are functions of drainage area and mean annual precipitation for the area [36]. The return periods ranged from 1.8 to 8.9 years according to the watershed. It was found that the flood event for the average return period of 3.6 years was caused by the AR event (15–18 February). There was almost no difference in the flood frequency between the upstream and downstream watersheds. The return periods in the upstream parts of watersheds 1 to 3 were 3.8, 3.1, and 2.4 years, respectively, and that of the downstream part of watershed 8 was 2.1 years. The factors affecting streamflow include not only the volume, but also the velocity, which reflect the geographic features such as the slope and width of the stream. The maximum and mean velocities of the streamflow were simulated for the stations in the eight watersheds. The simulated ranges of the maximum and mean velocities were 0.18–3.56 m/s and 0.11–1.80 m/s, respectively. The results of the streamflow velocity simulation were relatively high in the upstream areas, compared to the downstream, indicating that the streams in upstream area have a steeper slope and a narrower width.

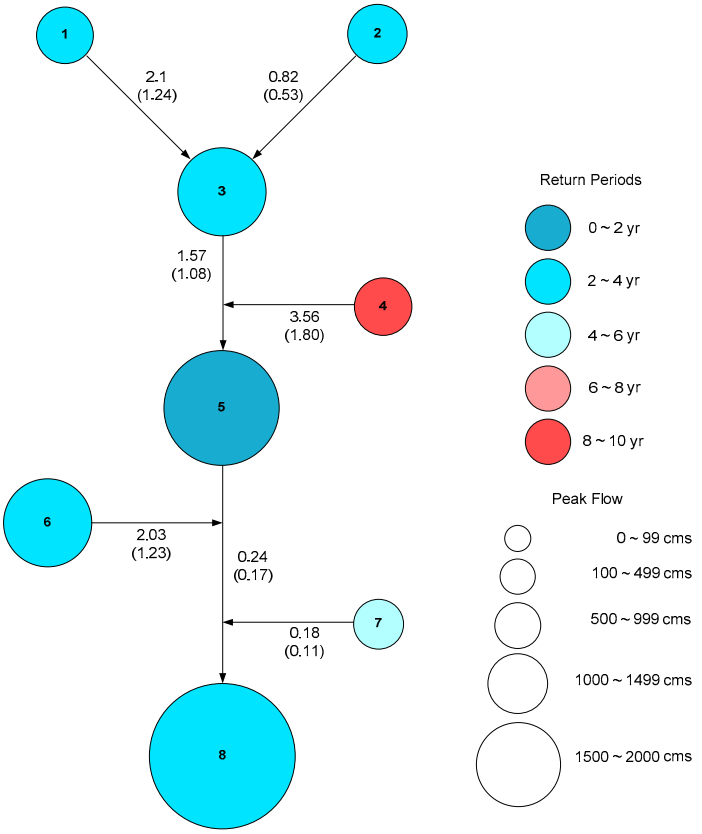

Figure 10. Results of streamflow simulations for sub-basins. The circle size and color indicate the magnitude of the peak flow and the return period for each sub-basin, respectively. The number on the arrow shows the maximum streamflow velocity (mean velocity, m/s).

4. Summary and Conclusions

This study aimed to introduce the NWM for analyzing the impacts of an AR event on hydrological responses and to present the analysis results. For this purpose, an AR event occurring during 15–18 February 2004 on the Russian River basin, California was selected as a case study. Among hydrological factors that play important roles in occurring flood generation, soil water content, direct runoff depth, and streamflow simulated by the NWM were used.

For validating the NWM performance for streamflow and soil water contents, various error metrics were used. The results showed that the NWM simulated the trends of streamflow better than the peak flow. The error metrics indicated that the average CC was 0.81, NSE was 0.47, PBIAS was 30%, PF was 31%, and TP was 4.5 h for streamflows. For soil water contents, the simulation results showed better performance in the wet season. The average CC was 0.92, NSE was −0.07, and BS was 106%. It was also showed that the NWM simulated trends well for soil water contents.

The major fundamental hydrological impact of the AR was a change in soil water contents of the top and deep soil layers which determine infiltration and percolation rates due to a long duration of rainfall with multiple pulses, and the AR decreased the infiltration rate of the topsoil layer due to the interaction with percolation process. The change also affected surface flow (e.g., direct runoff and streamflows). The saturated topsoil layer made surface flow high compared to the amount of precipitation during the AR event. The ratio of direct runoff depth to precipitation was 25% higher than the period when the soil was not saturated. This may cause flood volume with a return period of up to 8.9 years in the Russian river basin.

The NWM is able to accurately simulate the hydrological processes enhanced by AR events which can cause flooding. It is also effective in predicting the hydrological impacts of ARs, as well as the retrospective analysis. The NWM will play a critical role in hydrologic forecasting and enabling

the efficient management of water resources on the US west coast where ARs with complex heavy rainfalls and long durations occur frequently. Finally, the significance of soil water contents to extreme flood runoff should be emphasized: soil water content monitoring could aid in improving flood forecasting accuracy.

Author Contributions: Conceptualization, H.H. and J.K.; methodology, H.H. and J.K.; software, H.H. and J.K.; validation, H.H. and J.K.; formal analysis, H.H. and J.K.; investigation, H.H. and J.K.; resources, J.C.; data curation, S.L.; writing—original draft preparation, H.H. and J.K.; writing—review and editing, H.H., J.K., J.C., S.L., and V.C.; visualization, H.H. and J.K.; supervision, J.C., S.L., and V.C.; project administration, V.C.; funding acquisition, S.L., and V.C.

Funding: Funding for this study was provided by the California Department of Water Resources and the NOAA Physical Sciences Division, and this research was supported by the Basic Science Research Program through the National Research Foundation of Korea.

Acknowledgments: We appreciate the internal reviewer contribution from Rob Cifelli. Kim and Chandrasekar acknowledge support from NOAA Hydro-meteorological research program.

Conflicts of Interest: The authors declare no conflict of interest.

References

1. Zhu, Y.; Newell, R.E. Atmospheric rivers and bombs. *Geophys. Res. Lett.* **1994**, *21*, 1999–2002. [CrossRef]
2. Zhu, Y.; Newell, R.E. A proposed algorithm for moisture fluxes from atmospheric rivers. *Mon. Weather Rev.* **1998**, *126*, 725–735. [CrossRef]
3. Ralph, F.M.; Neiman, P.J.; Wick, G.A. Satellite and CALJET aircraft observations of atmospheric rivers over the eastern North Pacific Ocean during the winter of 1997/98. *Mon. Weather Rev.* **2004**, *132*, 1721–1745. [CrossRef]
4. Gimeno, L.; Nieto, R.; Vázquez, M.; Lavers, D.A. Atmospheric rivers: A mini-review. *Front. Earth Sci.* **2014**, *2*, 2. [CrossRef]
5. Ralph, F.M.; Neiman, P.J.; Wick, G.A.; Gutman, S.I.; Dettinger, M.D.; Cayan, D.R.; White, A.B. Flooding on California's Russian River: Role of atmospheric rivers. *Geophys. Res. Lett.* **2006**, *33*. [CrossRef]
6. Neiman, P.J.; Schick, L.J.; Ralph, F.M.; Hughes, M.; Wick, G.A. Flooding in western Washington: The connection to atmospheric rivers. *J. Hydrometeorol.* **2011**, *12*, 1337–1358. [CrossRef]
7. Hu, H.; Dominguez, F.; Wang, Z.; Lavers, D.A.; Zhang, G.; Ralph, F.M. Linking atmospheric river hydrological impacts on the US West Coast to Rossby wave breaking. *J. Clim.* **2017**, *30*, 3381–3399. [CrossRef]
8. Stohl, A.; Forster, C.; Sodemann, H. Remote sources of water vapor forming precipitation on the Norwegian west coast at 60 N–a tale of hurricanes and an atmospheric river. *J. Geophys. Res. Atmos.* **2008**, *113*. [CrossRef]
9. Lavers, D.A.; Villarini, G. The nexus between atmospheric rivers and extreme precipitation across Europe. *Geophys. Res. Lett.* **2013**, *40*, 3259–3264. [CrossRef]
10. Mundhenk, B.D.; Barnes, E.A.; Maloney, E.D. All-season climatology and variability of atmospheric river frequencies over the North Pacific. *J. Clim.* **2016**, *29*, 4885–4903. [CrossRef]
11. Hirota, N.; Takayabu, Y.N.; Kato, M.; Arakane, S. Roles of an atmospheric river and a cutoff low in the extreme precipitation event in Hiroshima on 19 August 2014. *Mon. Weather Rev.* **2016**, *144*, 1145–1160. [CrossRef]
12. Kamae, Y.; Mei, W.; Xie, S.P. Climatological relationship between warm season atmospheric rivers and heavy rainfall over East Asia. *J. Met. Soc. Jpn. Ser. II* **2017**, *95*, 411–431. [CrossRef]
13. Available online: https://www.noaa.gov (accessed on 15 April 2019).
14. Demaria, E.; Dominguez, F.; Hu, H.; von Glinski, G.; Robles, M.; Skindlov, J.; Walter, J. Observed hydrologic impacts of landfalling atmospheric rivers in the Salt and Verde river basins of Arizona, United States. *Water Resour. Res.* **2017**, *53*, 10025–10042. [CrossRef]
15. Espinoza, V.; Waliser, D.E.; Guan, B.; Lavers, D.A.; Ralph, F.M. Global Analysis of Climate Change Projection Effects on Atmospheric Rivers. *Geophys. Res. Lett.* **2018**, *45*, 4299–4308. [CrossRef]
16. Zhang, W.; Villarini, G. Uncovering the role of the East Asian jet stream and heterogeneities in atmospheric rivers affecting the western United States. *Proc. Natl. Acad. Sci. USA* **2018**, *115*, 891–896. [CrossRef]
17. Rutz, J.J.; Steenburgh, W.J.; Ralph, F.M. Climatological characteristics of atmospheric rivers and their inland infiltration over the western United States. *Mon. Weather Rev.* **2017**, *142*, 905–921. [CrossRef]

18. Lamjiri, M.A.; Dettinger, M.D.; Ralph, F.M.; Guan, B. Hourly storm characteristics along the US West Coast: Role of atmospheric rivers in extreme precipitation. *Geophys. Res. Lett.* **2017**, *44*, 7020–7028. [CrossRef]
19. Lavers, D.A.; Villarini, G. Atmospheric Rivers and Flooding over the Central United States. *J. Clim.* **2013**, *26*, 7829–7836. [CrossRef]
20. Nayak, M.A.; Villarini, G.; Lavers, D.A. On the skill of numerical weather prediction models to forecast atmospheric rivers over the central United States. *Geophys. Res. Lett.* **2014**, *41*, 4354–4362. [CrossRef]
21. Guan, B.; Waliser, D.E. Detection of atmospheric rivers: Evaluation and application of an algorithm for global studies. *J. Geophys. Res. Atmos.* **2015**, *120*, 12514–12535. [CrossRef]
22. Ralph, F.M.; Coleman, T.; Neiman, P.J.; Zamora, R.J.; Dettinger, M.D. Observed impacts of duration and seasonality of atmospheric-river landfalls on soil moisture and runoff in coastal northern California. *J. Hydrometeorol.* **2013**, *14*, 443–459. [CrossRef]
23. Young, A.M.; Skelly, K.T.; Cordeira, J.M. High-impact hydrologic events and atmospheric rivers in California: An investigation using the NCEI Storm Events Database. *Geophys. Res. Lett.* **2017**, *44*, 3393–3401. [CrossRef]
24. Cifelli, R.; Chandrasekar, V.; Chen, H.; Johnson, L.E. High resolution radar quantitative precipitation estimation in the San Francisco Bay area: Rainfall monitoring for the urban environment. *J. Met. Soc. Jpn. Ser. II* **2018**, *96*, 141–155. [CrossRef]
25. Kim, J.; Johnson, L.E.; Cifelli, R.; Coleman, T.; Herdman, L.; Martyr-Koller, R.; Finzi-Hart, J.; Erikson, L.; Barnard, P.L. *San Francisco Bay Integrated Flood Forecasting Project Summary Report*; NOAA Technical Memorandum PSD-317; NOAA Printing Office: Silver Spring, MD, USA, 2018.
26. Available online: http://water.noaa.gov/about/nwm (accessed on 15 April 2019).
27. Available online: https://ral.ucar.edu/projects/wrf_hydro/overview (accessed on 15 April 2019).
28. Available online: https://ral.ucar.edu/projects/supporting-the-noaa-national-water-model (accessed on 15 April 2019).
29. White, A.B.; Neiman, P.J.; Ralph, F.M.; Kingsmill, D.E.; Persson, P.O.G. Coastal orographic rainfall processesobserved by radar during the California Land-Falling Jets Experiment. *J. Hydrometeorol.* **2003**, *4*, 264–282. [CrossRef]
30. Matrosov, S.Y.; Cifelli, R.; Neiman, P.J.; White, A.B. Radar rain-rate estimators and their variability due to rainfall type: An assessment based on hydrometeorology testbed data FROM the southeastern United States. *J. Appl. Meteorol. Clim.* **2016**, *55*, 1345–1358. [CrossRef]
31. Willie, D.; Chen, H.; Chandrasekar, V.; Cifelli, R. Evaluation of multisensor quantitative precipitation estimation in Russian river basin. *J. Hydrol.* **2016**, *22*, 1–11. [CrossRef]
32. Dettinger, M.D.; Ralph, F.M.; Das, T.; Neiman, P.J.; Cayan, D.R. Atmospheric rivers, floods and the water resources of California. *Water* **2011**, *3*, 445–478. [CrossRef]
33. Kim, J.; Han, H.; Johnson, L.E.; Lim, S.; Cifelli, R. Hybrid machine learning framework for hydrological assessment. *J. Hydrol.* **2019**, *577*, 123913. [CrossRef]
34. Available online: http://prism.oregonstate.edu/ (accessed on 30 April 2019).
35. Kim, J.; Johnson, L.; Cifelli, R.; Choi, J.; Chandrasekar, V. Derivation of Soil Moisture Recovery Relation Using Soil Conservation Service (SCS) Curve Number Method. *Water* **2018**, *10*, 833. [CrossRef]
36. Gotvald, A.J.; Barth, N.A.; Veilleux, A.G.; Parrett, C. *Methods for Determining Magnitude and Frequency of Floods in California, Based on Data through Water Year 2006*; Scientific Investigations Rep. 2012-5113; U.S. Dept. of the Interior, U.S. Geological Survey: Reston, VA, USA, 2012.